THESIS

ENGINEERING A SILICON- PHOTONIC BIMODAL BIOSENSOR

Submitted by

Ahmed Mohammad

Department of Electrical and Computer Engineering

In partial fulfillment of the requirements

For the Degree of Master of Science

Colorado State University

Fort Collins, Colorado

Fall 2024

Master's Committee:

Advisor: Mahdi Nikdast
Co-Advisor: Kevin Lear

Matthew Kipper

ABSTRACT

ENGINEERING A SILICON PHOTONIC BIMODAL BIOSENSOR

Biosensors are powerful analytical devices that integrate biological sensing elements with physicochemical transducers to detect and quantify specific analytes, offering wide-ranging applications in fields such as medical diagnostics, environmental monitoring, food safety, and drug discovery. Bimodal waveguide (BiMW) biosensors, an interferometric optical biosensor, proven to be one of the best optical biosensors based on their high sensitivity, real time detection and compact design. During its early development stages, early 2010's, the height of the bimodal waveguide was increased to induce interference between the fundamental and first-order modes. Later, in late 2010's, change in the width of the bimodal waveguide were introduced to induce this interference. Our novel design builds upon these advancements, focusing on optimizing some parameters, mainly the width of the bimodal biosensor, to enhance performance and sensitivity. Many attempts were simulated to get a high fringe visibility and to determine the reduction in the transmission monitor was due to reduce the input power or the change in the effective index in the sensing region. Then, we came out with a design with one input, to maximize the fringe visibility, and two output, to determine the source power fluctuation. Multiple changes in the parameters, such as the width and the offset of the input waveguide, were investigated. In addition, change in the width of the bimodal waveguide was also included in this experiment. Finally, we varied the gap between the two output bends. All these parameters were varied to get a higher fringe visibility and lead to better sensitivity. Moreover, we discovered that this design requires the sample to be placed on top of the bimodal waveguide,

rather than on the sides. We concluded that the best design we can extract is the one with 120 rad/RIU cm.

ACKNOWLEDGEMENTS

I would like to express my deepest gratitude to my advisor, Prof. Mahdi Nikdast, and my co-advisor, Prof. Kevin Lear, for their guidance, support, and mentorship throughout my thesis. They have been patient and encouraging every step of the way, and I am truly grateful for that. I would also like to thank Prof. Matt Kipper for serving as a part of my defense committee and for his time and effort in evaluating my thesis.

TABLE OF CONTENTS

ABSTRACT ii
ACKNOWLEDGEMENTS iv
CHAPTER ONE – INTRODUCTION 1
CHAPTER TWO – BACKGROUND AND LITERATURE REVIEW 3
2.1-Background 3
2.2-Types of biosensors 4
2.2.1-Microring resonator 4
2.2.2-Mach–Zehnder interferometer (MZI) 6
2.2.3-Bimodal waveguide biosensors (BiMW) 7
2.3-Literature Review 10
CHAPTER THREE – METHODS 14
CHAPTER FOUR – RESULTS AND DISCUSSION 20
CHAPTER FIVE – CONCLUSION 33
REFERENCES 35
APPENDICIES 37
I-Ansys Lumerical 37
II-Scripts 38
III-Effective indices for TE0 and TE1 for bimodal waveguide width 660nm 48
IV-Fitting coefficient values for all bimodal waveguide widths 51

CHAPTER ONE – INTRODUCTION

Bimodal waveguide (BiMW) biosensors are cutting-edge integrated optical devices that combine high sensitivity, compact design, and label-free detection capabilities, making them powerful tools for real-time biomolecular sensing in fields like medical diagnostics, environmental monitoring, and drug discovery. When combined with a bio-recognition element, it enables direct, label-free detection of biomolecular interactions. The BiMW sensor is manufactured using standard silicon-based technology, which ensures cost-effective production and meets the portability and disposability needs for point-of-care (POC) applications. Integrated photonic refractive index (RI) sensors typically rely on the evanescent tail of waveguide modes, and several configurations have been developed, including Mach-Zehnder interferometers (MZIs), Young interferometers, and microring resonators (MRR). Interferometer RI sensors, which have been a focus of research since the early stages, continue to thrive due to their notable benefits. These include exceptional sensitivity, and a low limit of detection (LOD).

In conventional interferometer RI sensors, the interference pattern is usually created by splitting the light into two distinct channels: a reference channel and a sensing channel. The reference channel remains unaffected by the external environment, while the sensing channel interacts with the surrounding medium, allowing changes in refractive index to be detected. When the light from both channels is recombined, any phase shift caused by variations in the sensing channel leads to interference, enabling precise measurement of refractive index changes. This dual-channel setup ensures high sensitivity and accuracy in detecting even small variations in the target substance.

Unlike traditional interferometer RI sensors, which rely on interference between separate reference and sensing channels, the bimodal waveguide interferometer operates through interference between two distinct modes within the same waveguide: the fundamental mode and the first higher-order mode. Both modes are sensitive to changes in the external environment, but they respond differently. This differential response leads to an accumulated phase shift between the two modes, which ultimately modulates the output power. This unique mode-based interaction allows the bimodal waveguide interferometer to achieve high sensitivity while maintaining a compact and efficient design, offering advantages for various sensing applications. [1]-[9]

One of the challenges we faced in the design stage is to design a device that can combine more than one configuration. Our device combined two types of interferometer RI sensors, traditional BiMW and MZI, with one input and two output bimodal waveguide interferometer RI sensor.

In Chapter two, we will talk briefly about interferometer RI sensor types, such as MRR, MZI and traditional BiMW. Later in the same chapter, we will talk about previous work done in the field. In Chapter three, we will mention the methods done in this experiment and what are the materials used. The result will be in Chapter four with the with the discussion as well. Finally, the conclusion in Chapter five. At the end of this document, we put the Appendices, which contains information about the software we used, the code script and errors we faced.

CHAPTER TWO – BACKGROUND AND LITERATURE REVIEW

2.1-Background

In all waveguide-based biosensors, it is essential for the propagated evanescent field to be fully confined within the waveguide. In an optical waveguide, light is contained by total internal reflection (TIR). When light encounters an interface between two media with different refractive indices, it undergoes both partial reflection and refraction as shown in *Figure 1* [2]. When a high refractive index core (n_{core}) is surrounded by lower refractive index surrounding materials (n_s and $n_{cladding}$), and light propagates along the waveguide's longitudinal axis at an angle θ that exceeds the critical angle for TIR,

$$\theta_C = \arcsin\left(\frac{n_S}{n_{core}}\right)$$

then, the light is confined within the waveguide core, preventing it from propagating into the cladding material [3]. In the case of designing a bimodal biosensor, the evanescent field tales need to be in the cladding, which means just a small portion of the evanescent field must extend into the cladding, causing the bimodal interference as shown in *Figure 1*.

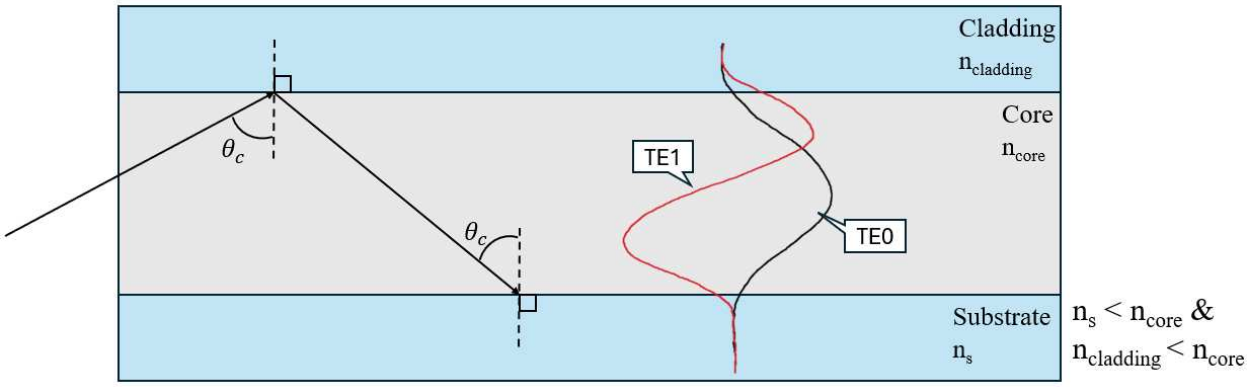

Figure 1 2-D figure for total internal reflection of an optical waveguide with TE0 and TE1 evanescent field.

2.2-Types of biosensors

2.2.1-Microring resonator

In a ring resonator, light is coupled from an input waveguide into a circular, ring-like waveguide shown in *Figure 2*. Within the circular waveguide, which is created by total internal reflection (TIR) along the curved surface of the ring, light circulates continuously, enabling efficient optical confinement and enhancing sensor performance. This repeated reflection leads to constructive interference over multiple roundtrips along the ring's circumference, significantly enhancing the sensor's sensitivity.. Detection in a ring resonator is based on changes in the refractive index according to the resonant condition:

$$\lambda = 2\pi \, . n_{eff} \frac{r}{m}$$

where m is an integer representing the angular momentum, λ is the wavelength, r is the radius of the ring, and n_{eff} is the effective refractive index.

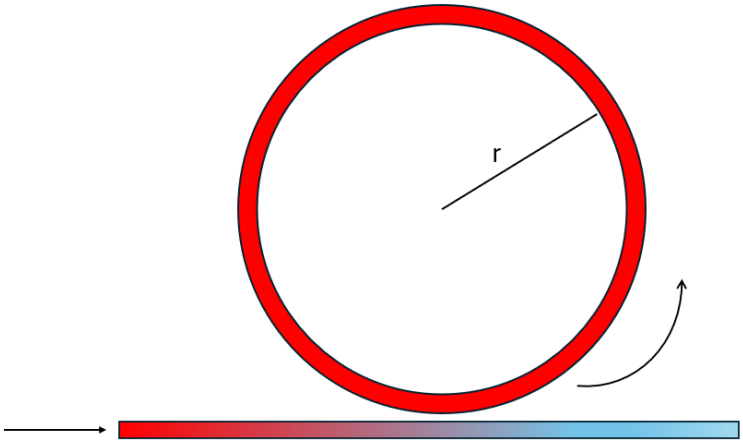

Figure 2 Ring resonator biosensor setup. light shows in red color travel from the input waveguide into the circular waveguide.

A change in the effective refractive index of the ring's environment causes a shift in the resonance spectrum, which can be detected by either scanning the wavelength or measuring the intensity profile at a specific wavelength. Unlike straight waveguides, the interaction in ring resonators is governed by the number of revolutions the light makes within the ring, which is represented as the resonator's quality factor (Q factor). The effective length (L_{eff}) is related to the Q factor by:

$$L_{eff} = Q \frac{\lambda}{2\pi \, . \, n}$$

where λ is the wavelength, and n is the refractive index of the ring resonator. High Q factors suggest low optical, resulting in narrow line-widths and high peak resolution, which correspond to increased sensitivity. This setup can achieve relatively high Q factors of 10^6. Ring resonator transducers are growing in popularity for biosensing applications due to their high sensitivity, capable of detecting refractive index changes as small as 10^{-7} refractive index units (RIU), and their potential for being fabricated in dense arrays for multiplexed analysis [2]. Various planar microcavity resonator configurations, such as microring, microdisk, and microtoroid resonators, have been implemented for biosensing applications since the early 2000s. These resonators, typically made from materials like Si3N4, SiO2, Si, and polymers, offer similar detection limits (DL) of around 10^{-5} to 10^{-7} RIU. However, most resonators, except for toroid resonators, exhibit relatively low Q-factors, especially in water-clad environments, due to optical losses such as side-wall scattering, bend radiation, mode mismatch, and material absorption. Recently, microsphere-based ring resonators and capillary-based opto-fluidic ring resonators (OFRR) have been developed, achieving Q-factors exceeding 10^6 and detection limits around 10^{-7} RIU. However, their three-dimensional architecture makes them unsuitable for on-chip fabrication and

integration with microfluidics, and their optical interrogation requires precise alignment of optical fibers [4].

2.2.2-Mach–Zehnder interferometer (MZI)

The Mach-Zehnder interferometer consists of a beamsplitter (Y-splitter), two arms (Reference and Sensor), and beam combiner (Y-splitter used backward). *Figure 3* shows the schematic diagram of the MZI. A light from a single source is split into two beams by the beamsplitter. Each beam follows a different path and then is combined at the second beamsplitter. The interference pattern formed when the two beams recombine can be used to detect differences in the optical length of the two arms, which can result from changes in the

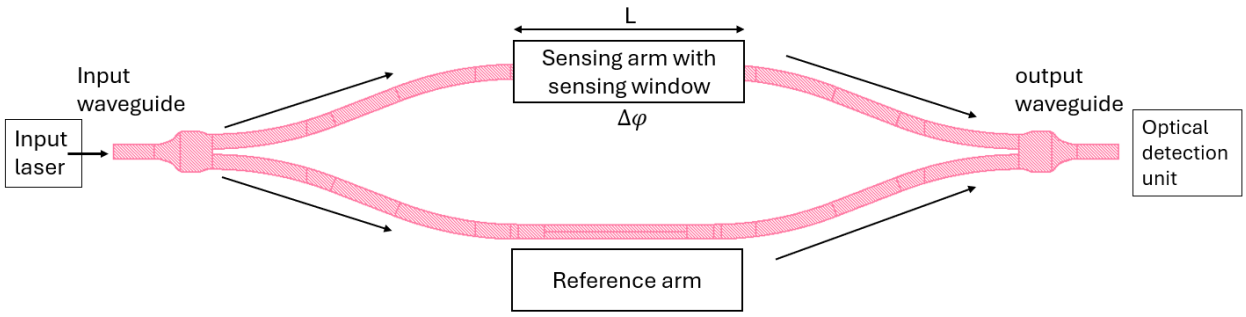

Figure 3 The schematic diagram of a typical Mach-Zehnder interferometer sensor based on optical waveguide [4]

refractive index of a material placed around the sensor arm. MZI can be used in biosensors due to its ability to detect the change in refractive index. The phase difference $\Delta\phi$ can be calculated using:

$$\Delta\phi = \frac{2\pi}{\lambda}\Delta N_{eff} L$$

where λ is the wavelength, ΔN_{eff} is the difference between the fundamental and the first order

mode effective refractive index and L is the length of the sensing window. We can measure the sensitivity of the MZI by using:

$$S = \frac{\Delta\phi}{\Delta n}$$

where, Δn represents the refractive index change of the sensing region, and $\Delta\phi$ is the phase change of the MZI sensor corresponding to a given Δn [5].

2.2.3-Bimodal waveguide biosensors (BiMW)

The bimodal waveguide biosensor is an advanced common-path interferometric sensor that leverages the evanescent field detection mechanism. It enables the direct, label-free detection of a wide range of biomolecular interactions using specific biorecognition elements. Thanks to its high sensitivity, the BiMW biosensor has been applied to monitor critical nucleic acid sequences, including mRNA transcripts and microRNAs, found in human samples at attomolar to femtomolar concentrations. This biosensor holds great potential as a diagnostic and prognostic tool for complex diseases like cancer, where these biomarkers are key indicators [6]. In the BiMW interferometer, laser light is initially coupled into a straight single-mode rib waveguide, which supports a single guided mode. This mode is then coupled into a bimodal rib waveguide by passing through a step-junction (modal splitter), causing it to split into two transverse modes with the same polarization. Figure 4 shows the structure of a BiMW device.

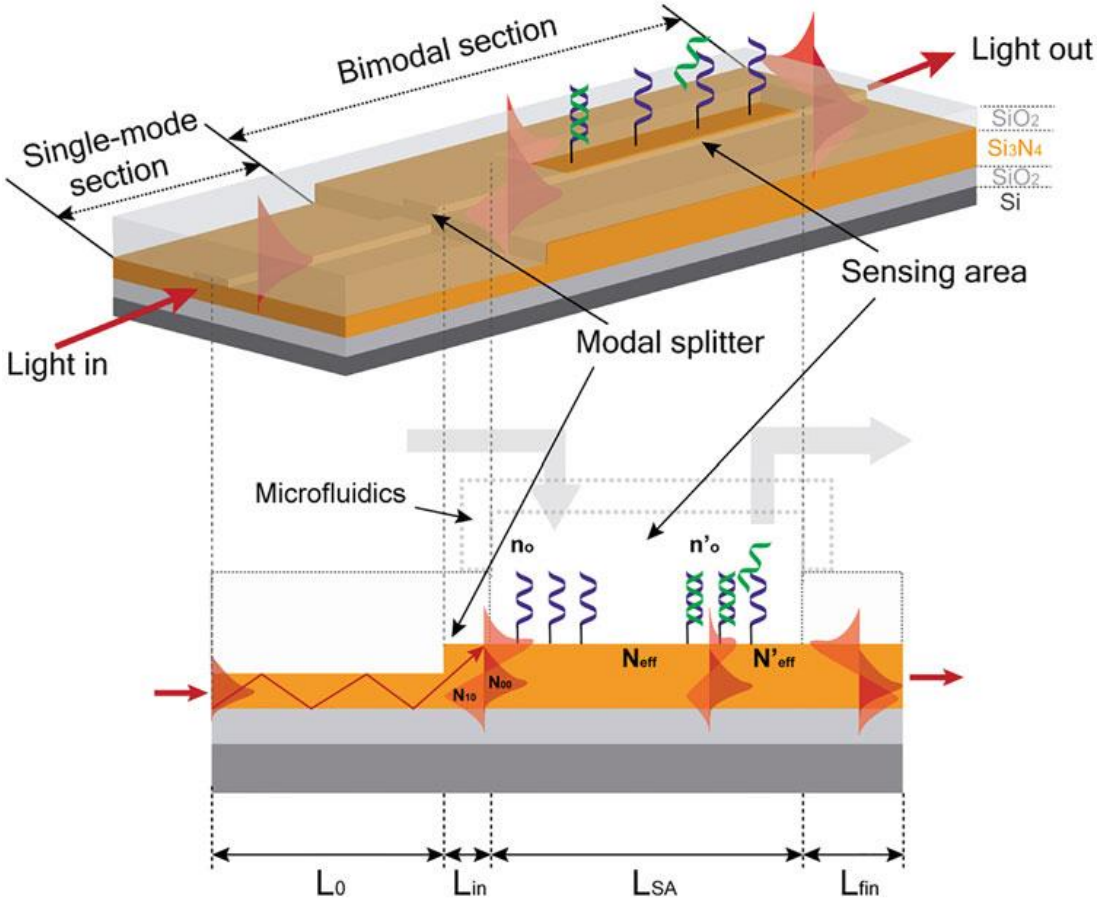

Figure 4 BiMW device structure and how it works 'Reproduced with permission from Springer Nature' [6]

A sensing region is exposed along the bimodal section of the waveguide, allowing the evanescent field generated by each mode to interact with the surrounding medium. The system is sensitive to changes in the refractive index of the environment. Since the two propagating modes share a common path but have different evanescent field profiles, any variation in the refractive index affects them differently, leading to the formation of an interference pattern at the output of the device. When a hybridization event occurs on the sensor surface between a DNA probe layer with refractive index n_0 and its complementary target sequence, the refractive index of the biosurface changes to n_0', as illustrated in *Figure 4*. This change in the external refractive index

impacts the effective refractive index of the propagating modes, resulting in a phase shift $\Delta\phi$ and can be calculated using:

$$\Delta\phi = 2\pi \frac{L_{SA}}{\lambda}(\Delta N_{10} - N_{00})$$

where N_{00} is for fundamental mode and N_{10} for first order mode, L_{SA} is the length of the sensor area and λ is the wavelength. This phase difference is measured by a two-section photodetector and is directly correlated to the concentration of the target sequence in the sample. The phase shift caused by the biomolecular interaction on the sensor surface is determined by analyzing the variation in the output intensity distribution by calculating the signal:

$$S_R = \frac{I_{up} - I_{down}}{I_{up} + I_{down}}$$

where I_{up} and I_{down} represent the intensities collected by the upper and lower sections of the detector, and the signal ratio S_R is typically expressed as a percentage. The BiMW interferometer has proven to be one of the most sensitive devices for label-free analysis, achieving detection sensitivity for bulk refractive index changes in the range of 10^{-7} to 10^{-8} RIU. This indicates its potential to detect biomolecular interactions at attomolar to femtomolar (aM–fM) concentrations. However, the limit of detection (LOD) is not determined solely by the sensor itself but also relies on a combination of three key factors: (1) the optimal design of nucleic acid-based probes, (2) their covalent attachment to the sensor surface (biofunctionalization process), and (3) the detection conditions used during nucleic acid hybridization [6].

2.3-Literature Review

A previous work done by [7], when they studied the effect of changing the offset of the input waveguide, which supports single transversal mode, to get the maximum fringe visibility. The operating principle of the bimodal waveguide interferometer is similar to MZI structures, however, in this case, interference occurs between two internal modes rather than between light from two separate arms. Light is first launched into the input waveguide and then coupled into two modes, fundamental transverse electric (TE0) and first order transverse electric (TE1), and radiation modes supported by the bimodal waveguide at the discontinuous junction. *Figure 5* shows the schematic of the device. The power ratio between the TE0 and TE1 modes can be controlled by adjusting the location of the input waveguide. Both modes propagate through the sensing region at different velocities, causing a phase difference to accumulate before they interfere at the second discontinuous junction. Since the two modes are affected differently by environmental conditions, the accumulated phase difference varies with the refractive index of the environment.

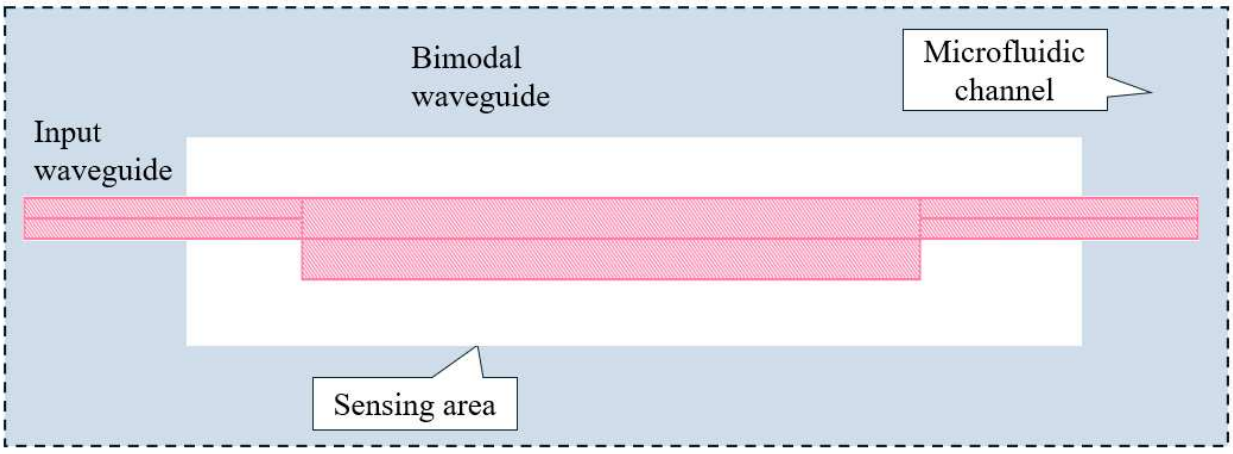

Figure 5 schematic of the bimodal RI biosensor

Consequently, changes in the refractive index of the surroundings can be detected by shifts in the transmission spectrum of the interferometer. To calculate the output power, we can use:

$$I_{out} = \frac{1}{2}(I_0 + I_1 + 2\sqrt{I_0 I_1}\cos(\Delta\varphi)$$

where I_0, $I_1$and I_{out} are the power of the fundamental, first order mode and output power, respectively. $\Delta\varphi$ is the accumulated phase difference between TE0 and TE1 after the sensing area. Fringe visibility γ, or visibility of interference fringes, refers to the contrast or clarity of the interference pattern (fringes) observed in an interferometer, and it can be expressed as:

$$\gamma = \frac{2\sqrt{I_0 I_1}}{I_0 + I_1}$$

From this formula, γ can be maximized when both modes TE0 and TE1 have the same power, and this can be done by adjusting the input offset S shown in *Figure 6*. From the figure, they showed that only TE0 will be excited when S=0 μm, and this means that the input waveguide

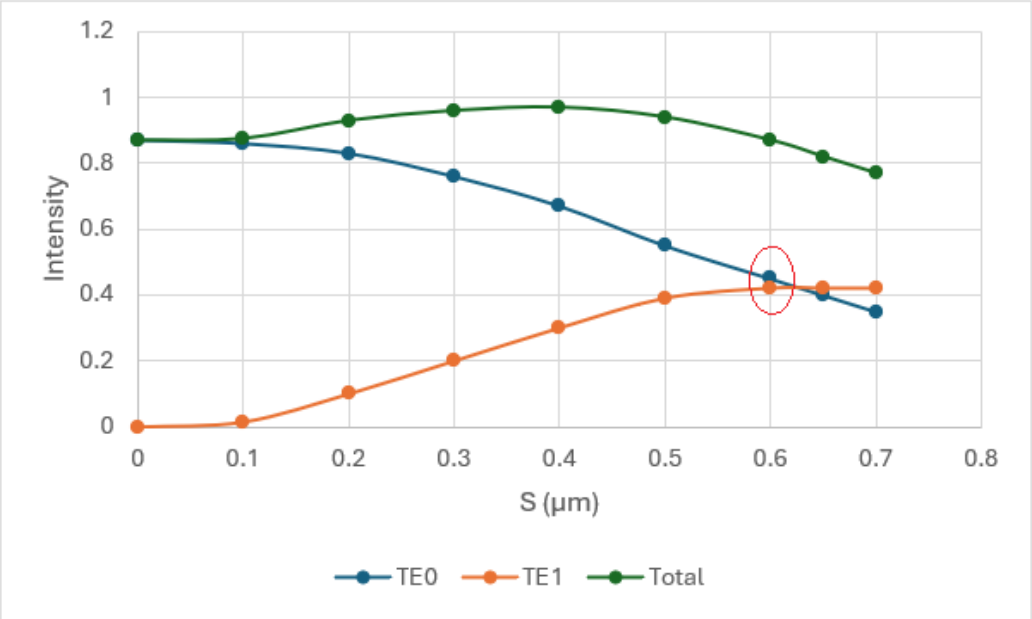

Figure 6 TE0 and TE1 mode power, and the total power vs offset S [8]

in the middle of the bimodal waveguide. When they increased S, TE1 power increased, but TE0 power decreased with a reverse relationship. At S=0.6 µm, both powers, TE0 and TE1, reached equal values which lead to maximum fringe visibility.

Another work done by [8], they showed that a compact photonic biosensor design using a perforated waveguide (PW) that performs as a bimodal interferometer (BiMI) had a 7.6 times better sensitivity than nonperforated BiMI. The investigation was done by comparing the performance between PW-BiMI, nonperforated BiMI and directional coupler (DC). They tested the three different configurations with length fixed at 100µm and analyzed the sensitivity of these configurations to refractive index changes. *Figure 7* shows the coupling length change ΔL_c between the three types of biosensors.

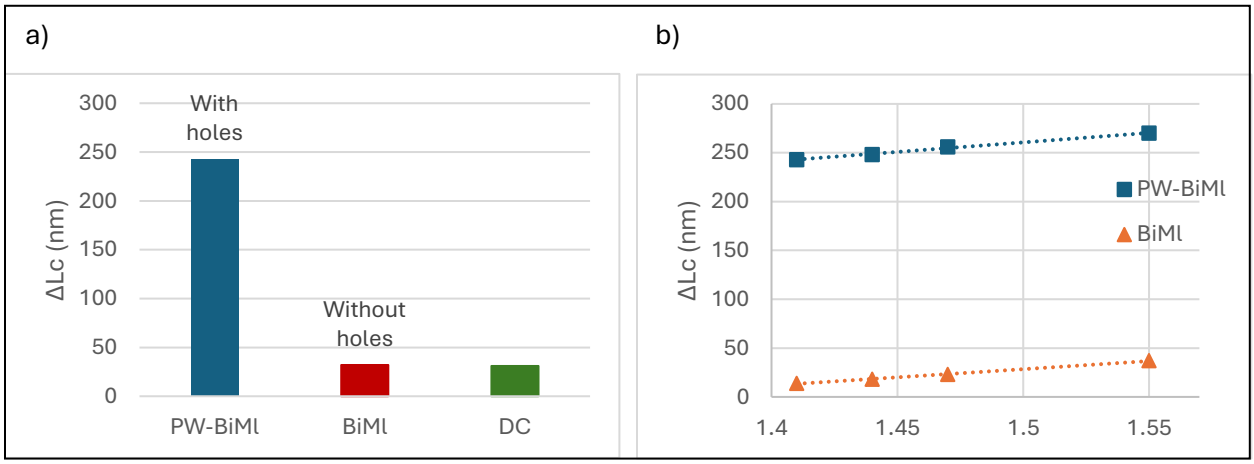

Figure 7 a) Coupling length change (ΔL_c) calculated for PW, BiMI, and DC sensors. b) Dependence of ΔL_c on the refractive index.

In [8], they investigate their device with two inputs (they only used one) and two outputs without investigating the input offset. Their design is inline with the bimodal part of the device. On the other hand, in [7], they investigate the position of the input (input offset) but with one output only. In our experiment, our device will combine both designs (one input and two output) with varying the input offset to determine the best sensitivity. Moreover, our device does not have

photodiode at the end of the device to measure the intensity. The motivation of using one input is to maximize the fringe visibility by varying the width and offset of the input waveguide. In addition, using two outputs instead of one output is to determine if it is a source power fluctuation or index change in the bimodal waveguide.

CHAPTER THREE – METHODS

BiMW is one type of biosensor that has been used for direct detection sensing purposes. Previous works done by [2], [6] and [9], used a vertical step junction by increasing the height of the waveguide to cause the bimodal behavior. Other works, like [7], did it horizontally by increasing the width of the waveguide to cause the bimodal behavior. Our device has a horizontal step junction. The reason for choosing the horizontal design is to reduce manufacturing complexity. To develop a BiMW biosensor, we need to investigate several design parameters, such as bimodal waveguide widths, input offset and width, and the gap between the two output bends and record the interaction between the fundamental and first order mode in the bimodal waveguide. After that, we can decide, based on the fringe visibility and sensitivity, which design is the best. Our device design parameters are tabulated in Table 1. We varied the width of the waveguide from 600nm to 850nm. In addition, we varied the width and the offset of the input.

Table 1: Device design parameters

PARAMETER	**SIZE**
INPUT WIDTH	300nm - 450nm
INPUT LENGTH	10μm
INPUT OFFSET	0nm - 150nm
BIMODAL WAVEGUIDE WIDTH	600nm - 850nm
BIMODAL WAVEGUIDE LENGTH	300μm / 1200μm
OUTPUT BEND WIDTH	450nm
OUTPUT BEND LENGTH	10μm
GAP BETWEEN OUTPUT BENDS	50-150nm
DEVICE HEIGHT	220nm
WAVELENGTH	1.55μm

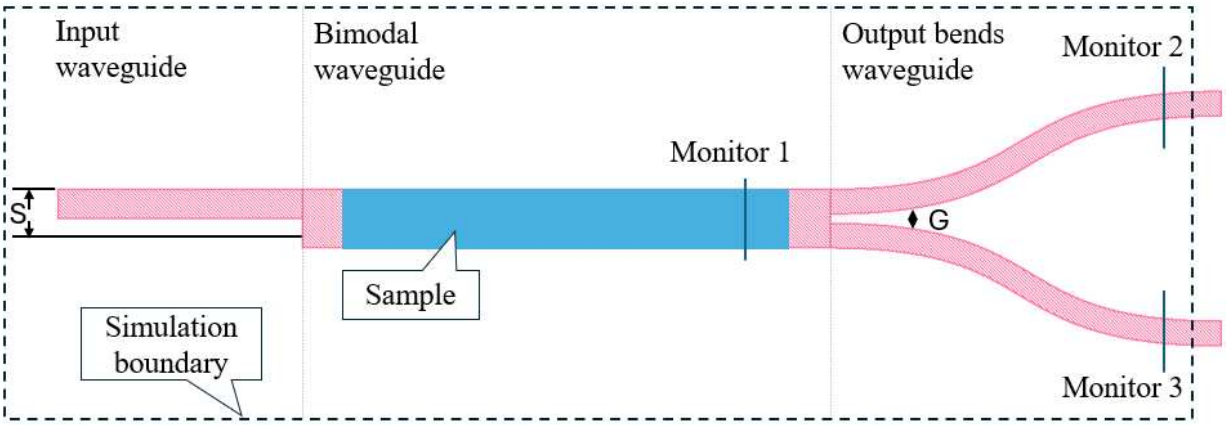

Figure 8 The main three parts of the device with monitors position

Table 2: Materials used in the simulations

MATERIAL	INDEX AT λ=1.55µm	PART
SILICON DIOXIDE (SiO2)	1.444	Substrate and cladding
SILICON (Si)	3.47	Core
SAMPLE	1.00 – 1.50	Sample on top of the core

The device structure consists of three parts, input waveguide, bimodal waveguide and two output bends as shown in *Figure 8.* Device 2D and 3D cross section and more details are shown in *Figure 9.* The materials used in the device are shown in *Table 2.* The sample index range from 1.00-1.50 was selected to cover typical values, with water having an index of ~1.3,and allowing for changes due to protein presence within this range After multiple attempts, when the sample was surrounding or on one side of the bimodal waveguide, we discovered that there was unusual oscillating in the output in our index range. *Figure 10* shows how the output oscillated when the sample was put around or on the side of the bimodal waveguide. Therefore, the sample was positioned on only top of the bimodal waveguide with sample thickness=2µm and width equal to the width of the bimodal waveguide. All the simulations and analyses were performed using Ansys Lumerical using varFDTD, a 2.5 variational finite-difference time-

domain (FDTD) solver with propagation in x-direction and using a non-uniform mesh setting. The number of mesh cells were 800 cells in y and z direction and minimum mesh step value = 1e-05µm as shown in *Figure 11*. The data were recorded using two methods, varFDTD and Finite-Difference Eigenmode (FDE) solvers. See *Appendix I* for more information about these two methods. Due to small back reflection from the ends of the output branches in the simulations, the simulation boundary had been placed before those branches ended. In other words, the device output terminated after the FDTD boundary to prevent the back reflection from the waveguide output as shown in *Figure 8*. The boundary condition that has been used in our simulations is perfectly matched layer (PML). PML is a better choice for our design to ensure better absorption and minimum reflection [13]. To build up the device using the software, we used the scripting language that the software supports. All the scripts can be found in *Appendix II.*

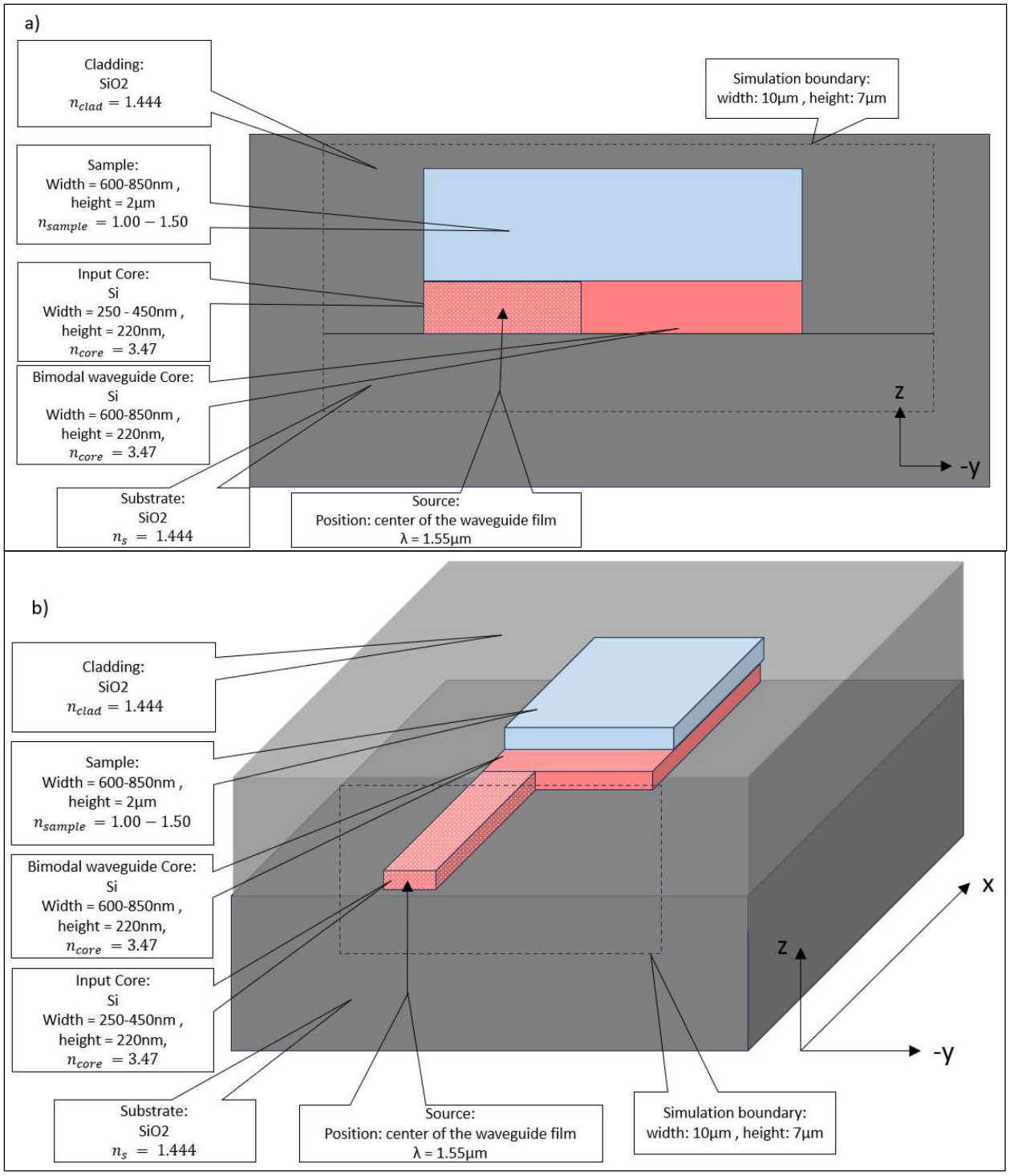

Figure 9 a) detailed 2D cross section of the device. b) detailed 3D cross section of the device

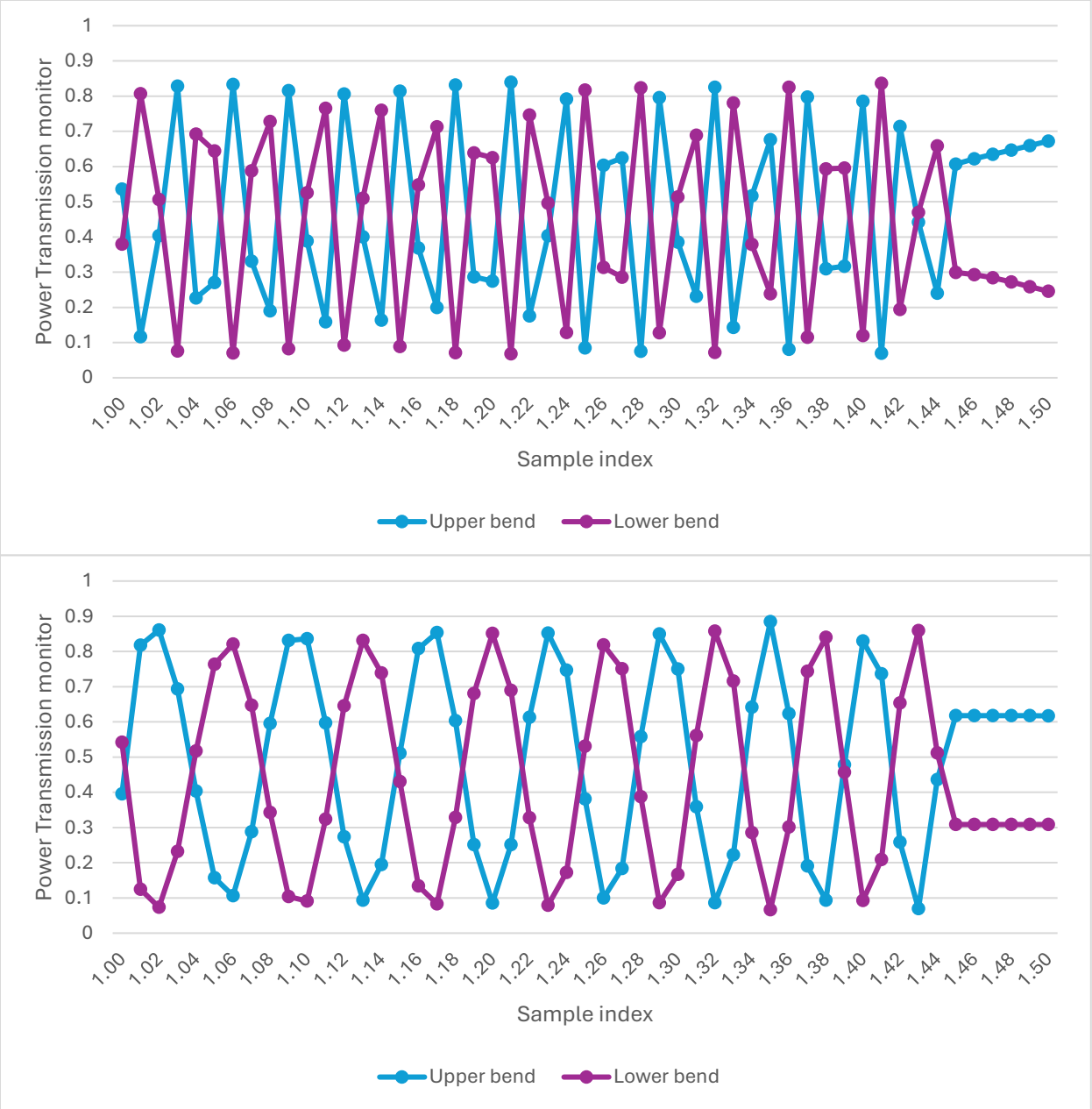

Figure 10 a) transmission output in the upper and lower bend when sample surrounding the bimodal waveguide b) transmission output in the upper and lower bend when sample on one side of bimodal waveguide

a)

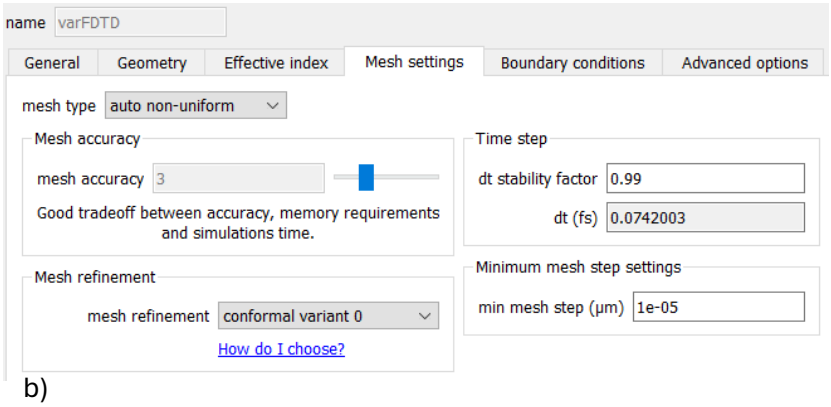

b)

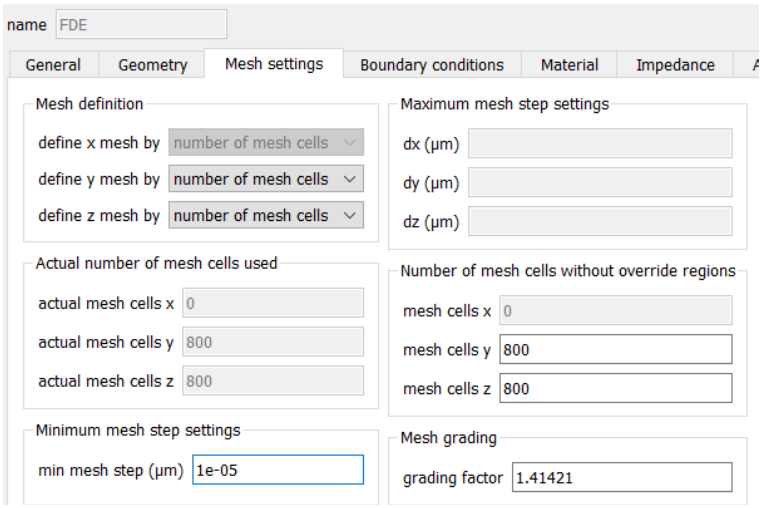

Figure 11 a) mesh setting for varFDTD. b) mesh setting for FDE

CHAPTER FOUR – RESULTS AND DISCUSSION

After applying the methods mentioned in the previous chapter, we put three transmission monitors in Ansys Lumerical varFDTD to calculate the transmission power (T), (more information in *Appendix I*), one in the bimodal waveguide and two in the upper and lower bend waveguides as shown in *Figure 8*. The reason behind putting one monitor in the bimodal waveguide is to see how much power loss we have in the two output waveguide bends and trying to reduce this loss. We started with bimodal waveguide length 300μm to check the transmission as we vary the index of the sample. *Figure 12.a-f* shows the transmission change with sample index for all six widths we have chosen for these simulations. We can see that none of them have a full 2π phase shift to calculate the fringe visibility, and only the 600 nm width has more than a π/2 phase shift. To make sure that we have the maximum and minimum transmission values for both output branches to determine the fringe visibility, we decided to simulate the device again with the longer length of 1200μm. *Figure 13.a-f* shows the transmission change with the sample index for all six widths with length 1200μm. As we increase the bimodal waveguide width, we introduce more disturbance due to increasing the modes supported inside the bimodal waveguide. Although that we don't have a 2π phase shift in these simulations, but we can see the maximum and minimum transmission, and we can calculate the modulation depth based on the equation:

$$modulation\ depth = transmission_{max} - transmission_{min}$$

where $transmission_{max}$ and $transmission_{min}$ are the maximum and minimum transmission values found for each width. Modulation Depth represents the absolute amplitude of the signal's transmission changes, while fringe visibility captures the relative contrast between maximum and

minimum intensities in the interference pattern. Fringe visibility reflects the quality of interference, while modulation depth reflects the magnitude of the signal. Higher fringe visibility often correlates with greater modulation depth, as better contrast in interference patterns usually results in a wide. We calculated the modulation depth for all the widths and the result tabulated in *Table 3*. After calculating the modulation depth, we change the simulation method from varFDTD to FDE to calculate the TE0 and TE1 and mode change between both of them.

Table 3: modulation depth calculation for each width

Bimodal Waveguide Width (nm)	**Maximum Transmission**	**Minimum Transmission**	**Modulation Depth**	**Sensitivity (rad/RIU cm)**	$\Delta n_{eff,TE0}$	$\Delta n_{eff,TE1}$
600	0.64	0.20	0.44	39.2	0.023	0.073
625	0.73	0.18	0.55	62	0.022	0.1
650	0.75	0.15	0.60	102.3	0.023	0.149
675	0.72	0.19	0.53	10	0.022	0.035
700	0.80	0.05	0.71	9.2	0.022	0.033
750	0.84	0.06	0.78	7.4	0.021	0.03
800	0.04	0.87	0.84	6.3	0.021	0.029
850	0.02	0.88	0.86	5.1	0.021	0.027

After that, we wanted to calculate the sensitivity of each width to calculate the performance of the device. Calculating the transverse electric (TE) modes using FDE is more convenient and faster compared to varFDTD in Ansys Lumerical. The performance of the device

is calculated using the equation:

$$Performance = modulation\ depth * Bulk\ sensitivity$$

and to calculate the bulk sensitivity, we need the phase difference ($\Delta\phi$) between the fundamental mode TE0 and first order mode TE1. We used the equation:

$$\Delta\phi = 2\pi\frac{L}{\lambda}(\Delta n_{\text{eff,TE1}} - \Delta n_{\text{eff,TE0}})$$

where L is the length of the bimodal waveguide, λ is the wavelength, $\Delta n_{\text{eff}} TE1$ is the change in first order mode effective index and $\Delta n_{\text{eff}} TE0$ is the change in fundamental mode effective index. After simulating through our sample index range (1.00-1.50) with increment step of 0.01 using FDE, we tabulate all the values of the effective indices of both modes, then we used the equation

$$S_{Bulk} = \frac{\Delta\phi}{L * \Delta n_c}$$

where S_{Bulk} is the bulk sensitivity and Δn_c is the change in refracting index of the sample on the device, to calculate the bulk sensitivity. After monitoring the TE0 and TE1, we calculated the sensitivity for all the bimodal waveguide widths and the result tabulated in *Table 3.* BiMW devices sensitivity increases as we increase the length of the device, so we put the sensitivity of the device regardless of the length of the device. *Figure 14.a* shows the modulation depth and sensitivity for different bimodal waveguide widths.

After knowing the highest sensitivity from the table above, now we need to investigate other parameters to get higher modulation depth. The next parameter we varied, is the input waveguide width with the bimodal waveguide width =650nm. We varied the input waveguide

width from 250nm to 450nm. *Figure 14.b* shows the modulation depth and sensitivity when we varied the input waveguide width. We saw that the input waveguide width = 350nm has the highest modulation depth value = 0.73. After that, we varied the input offset (S) as shown in *Figure 15.a*. We started with S=0nm, input waveguide inline with the bimodal waveguide, and increased the S value until we centered the input waveguide with the center of the bimodal waveguide. *Figure 15* shows the transmission when we varied S. In *Figure 15.b,* we clearly see that the inline configuration has the highest modulation depth and *Figure 15.f* has a modulation depth ≈ 0. In the first order mode, TE1, the electric field has a zero electric field intensity (or amplitude) at the center of the waveguide. This means that at the very center, S = 150nm, the magnitude of the electric field is zero. This is why we want to launch the source on the side of the waveguide. *Figure 14.c* shows the modulation depth and sensitivity for different input offset.

Table 4: Highest sensitivity and fringe visibility device parameters

PARAMETER	**SIZE**
INPUT WIDTH	350nm
INPUT LENGTH	10μm
INPUT OFFSET	0nm
BIMODAL WAVEGUIDE WIDTH	650nm
BIMODAL WAVEGUIDE LENGTH	1200μm
OUTPUT BEND WIDTH	450nm
OUTPUT BEND LENGTH	10μm
GAP BETWEEN OUTPUT BENDS	50nm
DEVICE HEIGHT	220nm
WAVELENGTH	1.55μm

After that, we continue to the next parameter with this configuration. The final parameter we varied is the gap between the two output waveguide bends (G) as shown in *Figure 16.a.* In *Figure 16.b-d,* we can see that as we increase G value, the modulation depth decreased, and that's due to an increase in the wall surface which increase the back reflection in the bimodal waveguide. *Figure 14.d* shows the modulation depth and sensitivity when we varied the gap between the two output bends. To compare, we simulated the device with the best configuration that we discovered using varFDTD with parameters tabulated in *Table 5.*

Table 5: sensitivity and performance comparison between the old and the new device configuration

DEVICE CONFIGURATION	SENSITIVITY (rad/RIU cm)	MAXIMUM TRANSMISSION	MINIMUM TRANSMISSION	MODULATION DEPTH	PERFORMANCE
OLD CONFIGURATION	102.3	0.75	0.15	0.60	61.65
NEW CONFIGURATION	102.3	0.81	0.076	0.73	74.64

After exploring these widths, we wanted to investigate even smaller steps, so we simulate bimodal waveguide width = 660nm. We did the exact same methods, varFDTD and FDE, we did for bimodal waveguide width 650nm. We started with input waveguide width 450nm, bimodal waveguide width 660 and bimodal waveguide length 1200nm. *Table 6* shows a comparison between bimodal waveguide width 650nm and 660nm.

Table 6: Comparison between device bimodal waveguide width 650nm and 660nm

Bimodal Waveguide Width (nm)	Maximum Transmission	Minimum Transmission	Modulation Depth	Sensitivity (rad/RIU cm)	$\Delta n_{eff,TE0}$	$\Delta n_{eff,TE1}$
650	0.75	0.15	0.60	102.3	0.023	0.149
660	0.76	0.13	0.63	120	0.023	0.17

We noticed that bimodal waveguide width 660nm has better sensitivity compared to width 650nm. Therefore, as we saw that input waveguide width 350nm is better than 450nm, we tried to simulate bimodal waveguide width with input width 350nm. We tabulated a comparison between input waveguide width of 450nm and 350nm for bimodal waveguide width of 660nm and the data shown in *Table 7.*

Table 7: comparison between input waveguide width of 450nm and 350nm for bimodal waveguide width 660nm

DEVICE CONFIGURATION	SENSITIVITY (rad/RIU cm)	MAXIMUM FRINGE	MINIMUM FRINGE	MODULATION DEPTH	PERFORMANCE
OLD CONFIGURATION	120	0.76	0.13	0.63	74
NEW CONFIGURATION	120	0.81	0.07	0.75	84

As we expected, the modulation depth increased with input waveguide width 350nm to 0.75. To visualize the sensitivity vs modulation depth for bimodal waveguide width 660nm, *Figure 14.e* shows the difference between input waveguide width 450nm and 350nm. See *Appendix III* for more information regarding the effective indices for the TE0 and TE1.

Finally, the output function of the bimodal waveguide biosensor achieved a fit with an R^2 value of 0.9986, indicating that the model explains 99.86% of the variance in the sensor's data. We need data from varFDTD, the transmission data, to calculate the fit function we obtain. The fit function that we have in *Figure 17* is base on the equation:

$$T_{fit,upper}(n_{sample}) = \frac{1}{2} T_{total}\,(1 - m\cos(2\Delta\Phi)),$$

where T_{total} is the total transmission when we added the maximum and minimum transmission in our sample range and m is the modulation depth. And to calculate the phase shift ΔΦ we used:

$$\Delta\Phi = 2\pi\left(a\left(n_{sample}\right)^2 + b\left(n_{sample}\right) + c\right), 1.00 \leq n_{sample} \leq 1.50$$

where a, b and c are the fitting coefficient or fitting parameters. After solving the coefficients, we got values a = 0.21, b = 0.28 and c = 1.48. *Appendix IV* contains fitting coefficient values for all widths. This high accuracy suggests that the BiMW output is closely aligned with the predicted behavior, demonstrating its reliability for sensitive measurements.

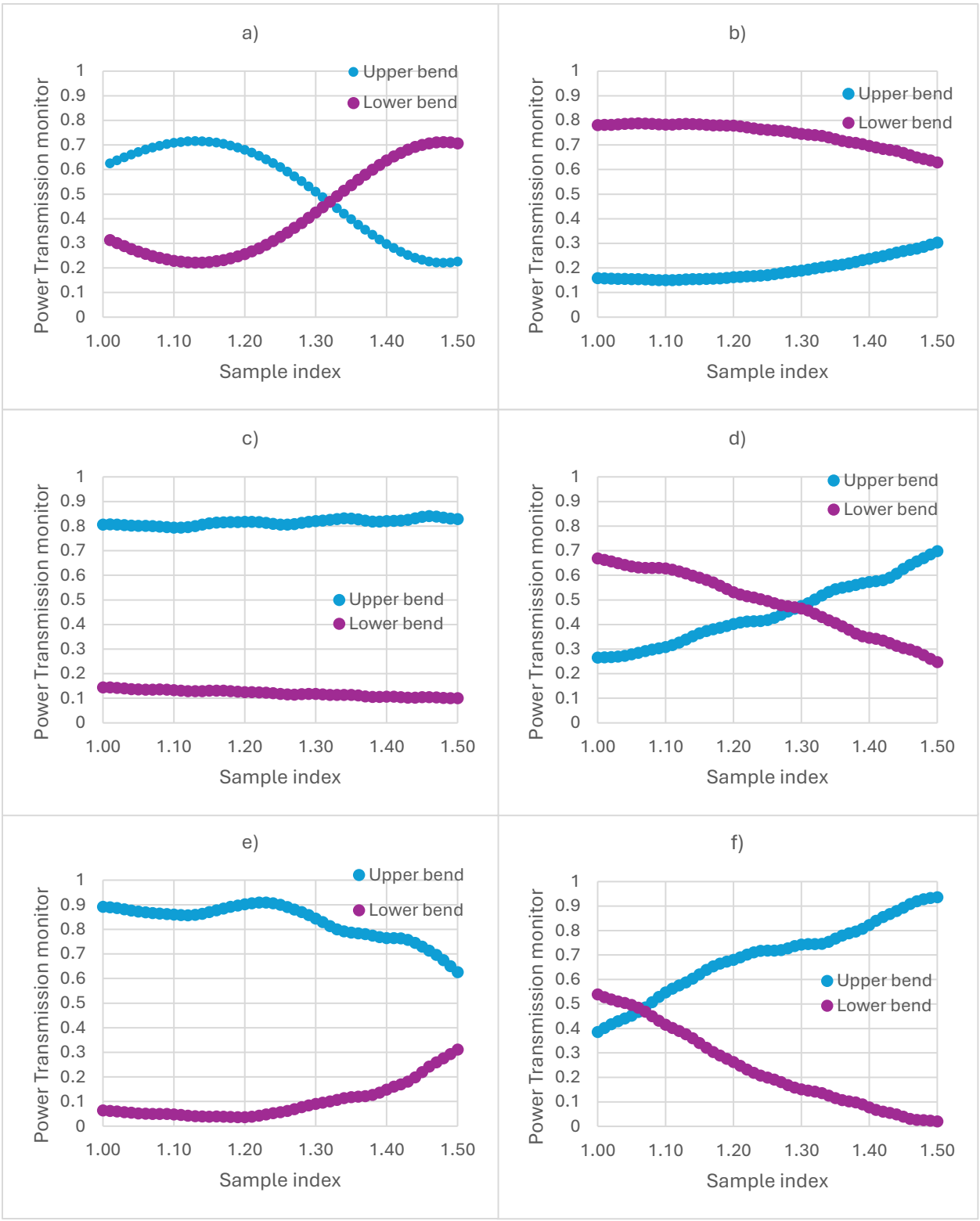

Figure 12 a) upper and lower output bends transmission for bimodal waveguide width=600nm and length 300μm b) upper and lower output bends transmission for bimodal waveguide width=650nm and length 300μm c) upper and lower output bends transmission for bimodal waveguide width=700nm and length 300μm d) upper and lower output bends transmission for bimodal waveguide width=750nm and length 300μm e) upper and lower output bends transmission power for bimodal waveguide width=800nm and length 300μm f) upper and lower output bends transmission power for bimodal waveguide width=850nm and length 300μm

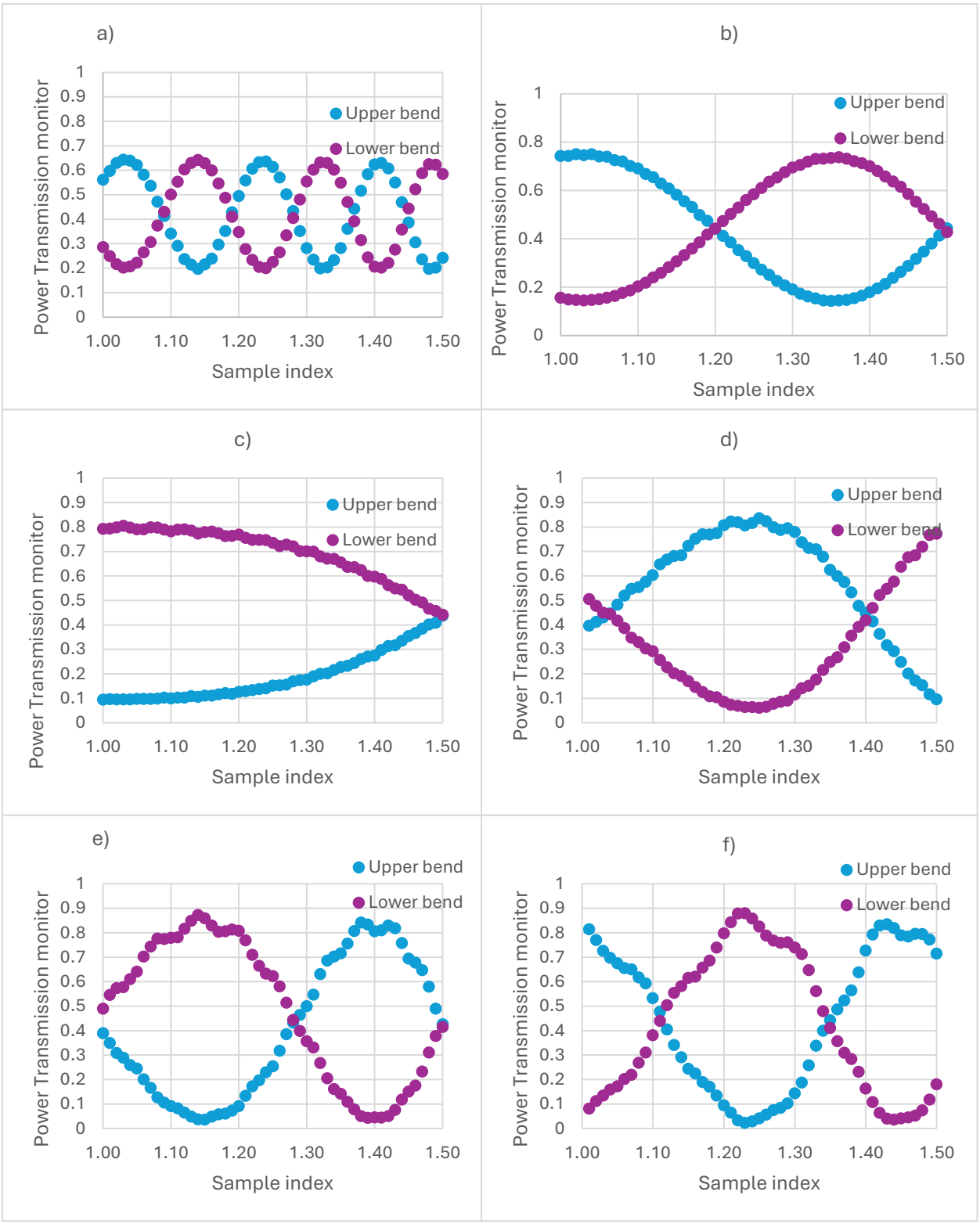

Figure 13 a) upper and lower output bends transmission for bimodal waveguide width=600nm and length 1200μm b) upper and lower output bends transmission for bimodal waveguide width=650nm and length 1200μm c) upper and lower output bends transmission for bimodal waveguide width=700nm and length 1200μm d) upper and lower output bends transmission for bimodal waveguide width=750nm and length 1200μm e) upper and lower output bends transmission for bimodal waveguide width=800nm and length 1200μm f) upper and lower output bends transmission for bimodal waveguide width=850nm and length 1200μm

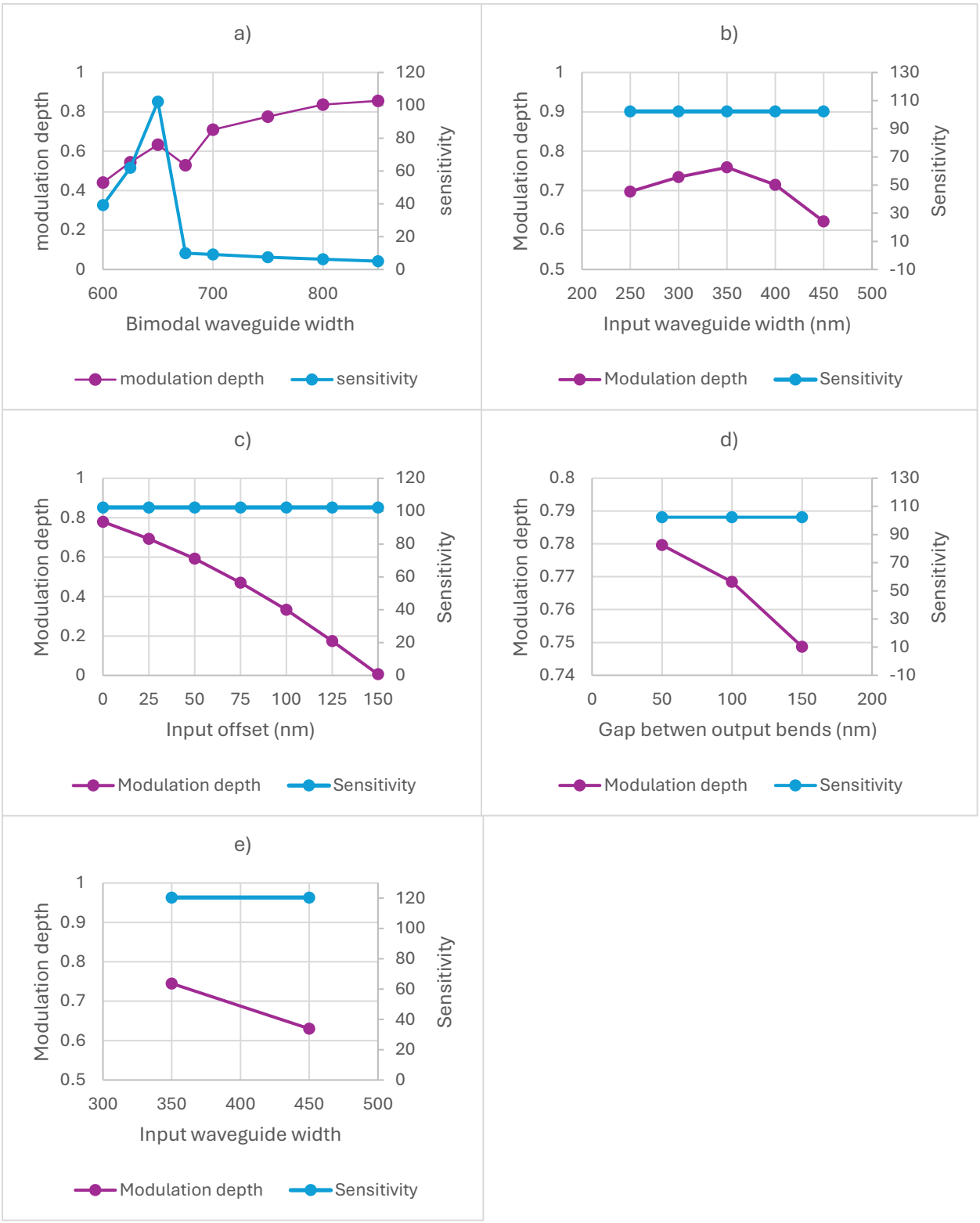

Figure 14 a) Modulation depth and sensitivity for bimodal waveguide width for length 1200μm b) Modulation depth and sensitivity for input waveguide width c) Modulation depth and sensitivity for input offset d) Modulation depth and sensitivity for the gap between the output bends e) modulation depth and sensitivity for two different input waveguide width for bimodal waveguide width 660nm.

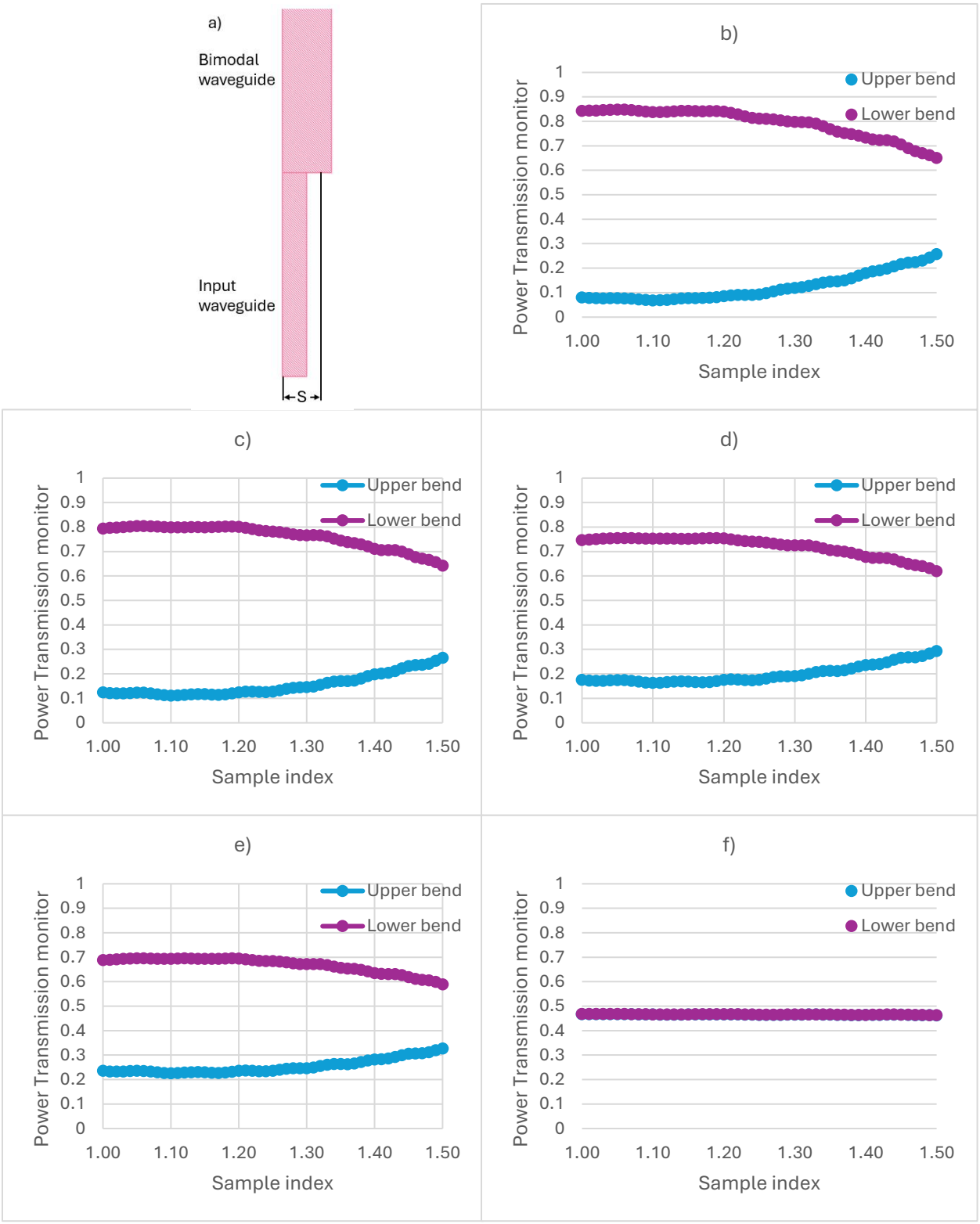

Figure 15 a) schematic of the input and wider waveguide offset b) upper and lower bends transmission for input waveguide offset S = 0nm c) upper and lower bends transmission for input waveguide offset S = 25nm d) upper and lower bends transmission for input waveguide offset S = 50nm e) upper and lower bends transmission for input waveguide offset S = 75nm f) upper and lower bends transmission for input waveguide offset S = 150nm

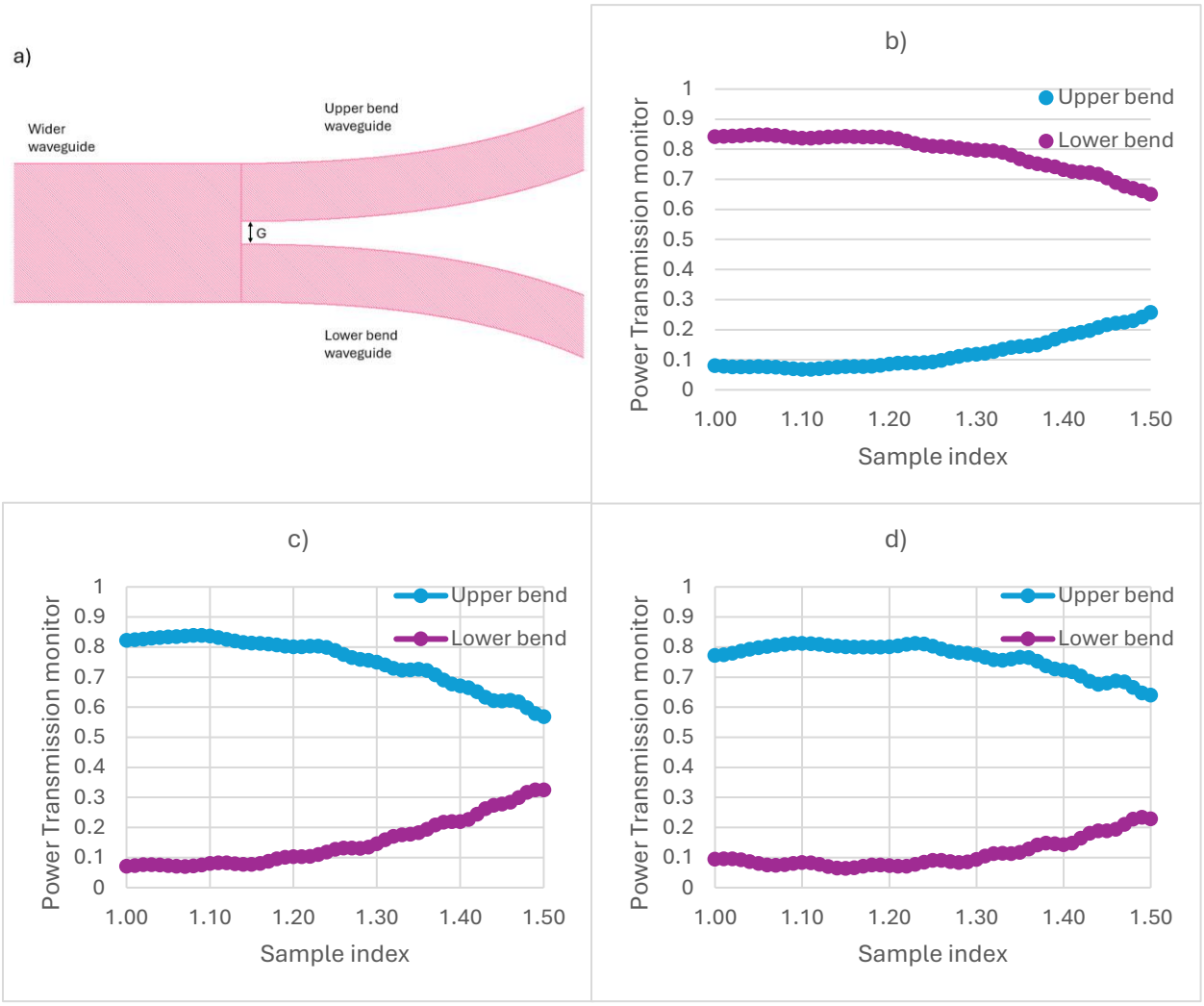

Figure 16 a) schematic of the gap between the two output bends. b) upper and lower bends transmission for gap G=50nm. c) upper and lower bends transmission for gap G=100nm d) upper and lower bends transmission for gap G=150nm

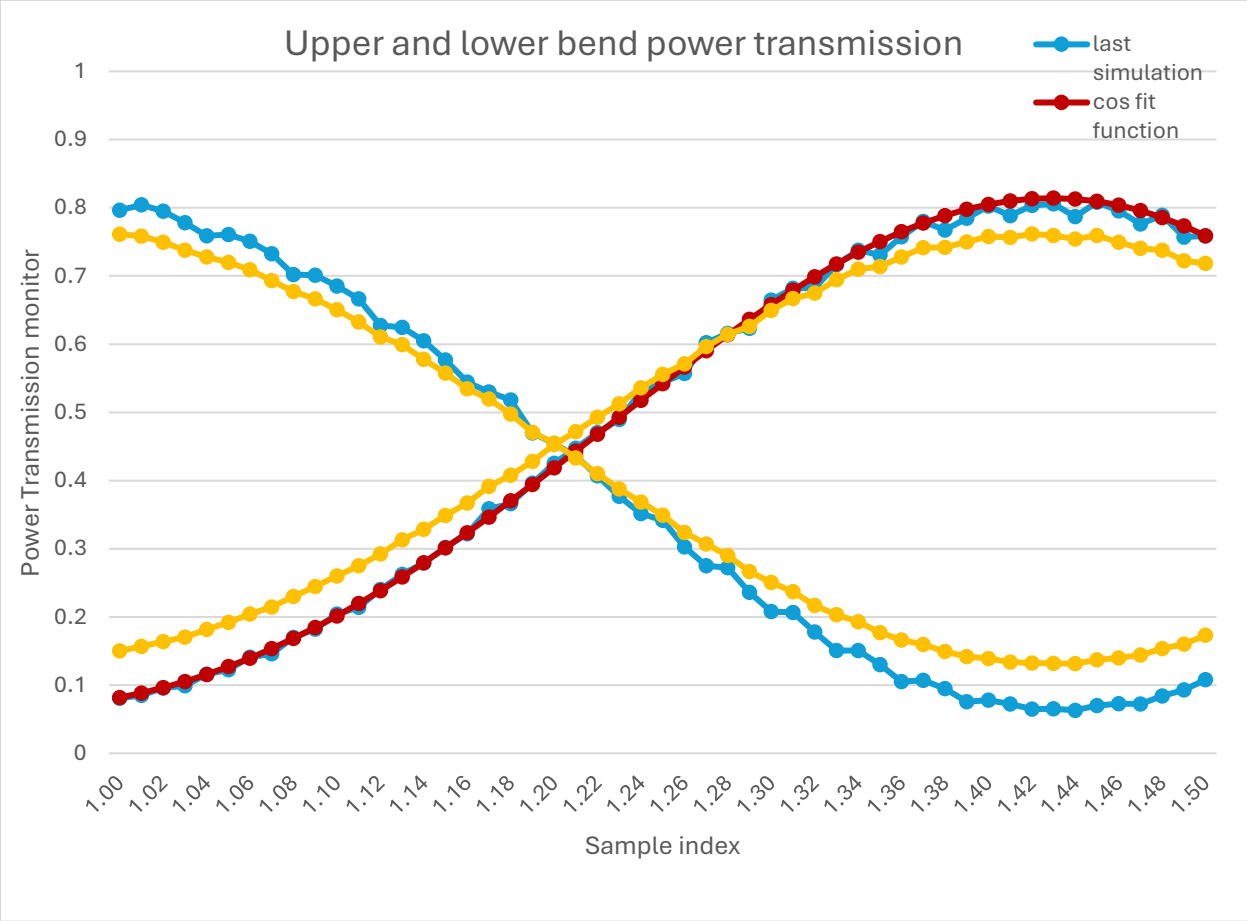

Figure 17 Comparison between the first and last simulation for length = 1200µm

CHAPTER FIVE – CONCLUSION

In this thesis, we presented a one input and two output BiMW with one thickness to insure less fabrication complexity and difficulties. This is a new BiMW design that combine two types of interferometers, BiMW, in the first and middle part, and MZI in the output part. With this design, we can investigate fringe visibility and source power fluctuation or index change in the bimodal waveguide. We investigated multiple variables to determine the best sensitivity out of our BiMW biosensor while varying the input offset and width, the bimodal waveguide width and the gap between the output bends. As we mentioned in chapter 2, the motivation for designing this device is to determine the best performance out of fringe visibility and sensitivity. Several methods were used to determine the best performance, such as varFDTD and FDE to calculate the transmission and mode indices respectively. The best configuration has sensitivity value = 120 rad/RIU cm, modulation depth = 0.75 and performance ≈ 84. The bimodal waveguide biosensor's output function exhibited an excellent fit, with a R^2 value of 0.9986, indicating that the model accounts for 99.86% of the data variability. This result highlights the sensor's high accuracy and reliability in capturing the expected response for precise measurements.

In future work, the research could focus on exploring variations in the width, length, and structure of the output waveguide bends to optimize the coupling efficiency and mode propagation in the bimodal waveguide biosensor. Further investigation around bimodal waveguide width 660nm could be considered to check the sensitivity of the device. Additionally, the fabrication process could be considered as the next step to test the device. Advanced lithography and etching techniques could be employed to minimize fabrication imperfections,

ensuring better alignment between the input and bimodal waveguides, and the bimodal waveguide and the output waveguide bends. Once fabricated, the device can be tested. Testing will focus on evaluating the sensor's sensitivity, stability, and ability to differentiate between fundamental and higher-order modes under different conditions such as temperature variation.

REFERENCES

[1] Luis Torrijos-Morán, Bárbara D. Lisboa, Maria Soler, Laura M. Lechuga, Je García-Rupérez, Integrated optical bimodal waveguide biosensors: Principles and applications, Results in Optics, Volume 9, 2022, 100285, ISSN 2666-9501, https://doi.org/10.1016/j.rio.2022.100285.

[2] González-Guerrero, A. B. (2013). Bimodal waveguide interferometer device based on silicon photonics technology for label-free and high sensitive biosensing. Universitat Autònoma de Barcelona.

[3] Schmidt, Holger & Hawkins, Aaron. (2008). Optofluidic waveguides: I. Concepts and implementations. Microfluidics and nanofluidics. 4. 3-16. 10.1007/s10404-007-0199-7.

[4] Luan, E.; Shoman, H.; Ratner, D.M.; Cheung, K.C.; Chrostowski, L. Silicon Photonic Biosensors Using Label-Free Detection. Sensors 2018, 18, 3519. https://doi.org/10.3390/s18103519.

[5] Yuan, D.; Dong, Y.; Liu, Y.; Li, T. Mach-Zehnder Interferometer Biochemical Sensor Based on Silicon-on-Insulator Rib Waveguide with Large Cross Section. Sensors 2015, 15, 21500-21517. https://doi.org/10.3390/s150921500

[6] Huertas, Cesar S, and Laura M Lechuga. “Ultrasensitive Label-Free Nucleic-Acid Biosensors Based on Bimodal Waveguide Interferometers.” Methods in molecular biology (Clifton, N.J.) vol. 2393 (2022): 89-125. doi:10.1007/978-1-0716-1803-5_6

[7] Y. Liang, M. Zhao, Z. Wu and G. Morthier, "Bimodal Waveguide Interferometer RI Sensor Fabricated on Low-Cost Polymer Platform," in IEEE Photonics Journal, vol. 11, no. 2, pp. 1-8, April 2019, Art no. 6801108, doi: 10.1109/JPHOT.2019.2900741

[8] K. Uchiyamada, K. Okubo, K. Asakawa, Y. Kamon, Y. Kitayama, T. Takeuchi, H. Suzuki, Perforated Bimodal Interferometric Biosensor for Affinity Sensing. Adv. Mater. Technol. 2019, 4, 1800533. https://doi.org/10.1002/admt.201800533

[9] S. Herranz, A. F. Gavelaand L. M. Lechuga, “Label-Free Biosensors Based on Bimodal Waveguide (BiMW) Interferometers”, in Methods in Molecular Biology, Methods in Molecular Biology, 2017, pp. 161–185. doi: 10.1007/978-1-4939-6848-0_11

[10] Mode - 2.5D varfdtd solver introduction, https://optics.ansys.com/hc/en-us/articles/360034917213-MODE-2-5D-varFDTD-solver-introduction (accessed Oct. 18, 2024).

[11] Mode - finite difference eigenmode (FDE) solver introduction – ansys optics, https://optics.ansys.com/hc/en-us/articles/360034917233-MODE-Finite-Difference-Eigenmode-FDE-solver-introduction (accessed Oct. 18, 2024).

[12] Transmission - script command – ansys optics, https://optics.ansys.com/hc/en-us/articles/360034405354-transmission-Script-command (accessed Oct. 18, 2024).

[13] PML boundary conditions in FDTD and mode, https://optics.ansys.com/hc/en-us/articles/360034382674-PML-boundary-conditions-in-FDTD-and-MODE (accessed Oct. 18, 2024).

APPENDICIES

I-Ansys Lumerical

According to [10], the varFDTD solver simplifies a 3D geometry into a 2D set of effective indices, enabling it to be solved using 2D FDTD. This approach is particularly effective for planar waveguide structures, as it assumes minimal coupling between the different supported slab modes. For devices like silicon on insulator (SOI) based slab waveguides, which typically support only two vertical modes with different polarizations, this assumption holds well.

Based on the information in [11], the Finite-Difference Eigenmode (FDE) solver analyzes the spatial profile and frequency behavior of modes by solving Maxwell's equations on a cross-sectional mesh of the waveguide, providing the mode field profiles, effective index, and loss.

For both types of simulations, the MODE Eigenmode Solver utilizes a rectangular Cartesian mesh. It's important to note that key simulation quantities, such as material properties, geometrical details, and electric and magnetic fields, are computed at each mesh point. While a finer mesh improves the accuracy of the device representation, it significantly increases both simulation time and memory usage [10][11].

According to [12], the T(f) formula calculates the amount of power transmitted through power monitors and profile monitors, normalized to the source power. A value of 0.5 indicates that 50% of the optical power from the source passes through the monitor. Negative values indicate that the power is going in the opposite direction. The power transmission in the frequency domain is determined using the following equation:

$$T(f) = \frac{\frac{1}{2}\int_{monitor} Re\big(P(f)\big).dS}{sourcepower(f)}$$

Where $T(f)$ is the normalized transmission as a function of frequency, $P(f)$ is the Poynting vector and dS represents the surface normal.

II-Scripts

All the scripts used to build and calculate the data can be found in this section.

i. Structure.lsf

```
# cladding structures
addrect;
set("name","SiO2");
set("x",600e-6);
set("x span",1300e-6);
set("x min",-50e-6);
set("x max",1250e-6);
set("y",0);
set("y span",20e-6);
set("y min",-10e-6);
set("y max",10e-6);
set("z",-2.555e-6);
set("z span",4.89e-6);
set("z min",-5e-6);
set("z max",-0.11e-6);
set("material","SiO2 (Glass) - Palik");
# core structures
addrect;
```

```
set("name","Si_input");
set("x",4.25e-6);
set("x span",11.5e-6);
set("x min",-1.5e-6);
set("x max",10e-6);
set("y",0.205e-6);
set("y span",0.35e-6);
set("y min",0.03e-6);
set("y max",0.38e-6);
set("z",0);
set("z span",0.22e-6);
set("z min",-0.11e-6);
set("z max",0.11e-6);
set("material","Si (Silicon) - Palik");
addrect;
set("name","Si_wide");
set("x",610e-6);
set("x span",1200e-6);
set("x min",10e-6);
set("x max",1210e-6);
set("y",0.05e-6);
set("y span",0.66e-6);
set("y min",-0.28e-6);
```

```
set("y max",0.38e-6);
set("z",0);
set("z span",0.22e-6);
set("z min",-0.11e-6);
set("z max",0.11e-6);
set("material","Si (Silicon) - Palik");
addwaveguide;
set("name","Si_output_upper_bend");
set("x",1210e-6);
set("y",0.3e-6);
set("z",0);
set("base width",0.45e-6);
set("base height",0.22e-6);
set("base angle",90);
pole = [0,0; 0.5,0; 2,1; 10,2]*1e-6;
set("poles",pole);
set("material","Si (Silicon) - Palik");
addwaveguide;
set("name","Si_output_lower_bend");
set("x",1210e-6);
set("y",-0.2e-6);
set("z",0);
set("base width",0.45e-6);
```

```
set("base height",0.22e-6);
set("base angle",90);
pole = [0,0; 0.5,0; 2,-1; 10,-2]*1e-6;
set("poles",pole);
set("material","Si (Silicon) - Palik");
addtriangle;
set("name","triangle_up");
vtx = [0,-0.095; 0.6,0.05; 0.6,-0.095]*1e-6;
set("vertices",vtx);
set("x",1209.4e-6);
set("y",0.475e-6);
set("z",0);
set("z span",0.22e-6);
set("z min",-0.11e-6);
set("z max",0.11e-6);
set("material","Si (Silicon) - Palik");
addtriangle;
set("name","triangle_down");
vtx = [0,0.195; 0.6,0.195; 0.6,0.05]*1e-6;
set("vertices",vtx);
set("x",1209.4e-6);
set("y",-0.475e-6);
set("z",0);
```

```
set("z span",0.22e-6);
set("z min",-0.11e-6);
set("z max",0.11e-6);
set("material","Si (Silicon) - Palik");
# sample structure
addrect;
set("name","Sample");
set("x",610e-6);
set("x span",1180e-6);
set("x min",20e-6);
set("x max",1200e-6);
set("y",0.05e-6);
set("y span",0.66e-6);
set("y min",-0.28e-6);
set("y max",0.38e-6);
set("z",1.11);
set("z span",2e-6);
set("z min",0.11e-6);
set("z max",2.11e-6);
set("material","Sample index"); #Need to be added manually in the material table
```

ii. monitors_source_FDTD.lsf

```
# add varFDTD
```

```
addvarfdtd;
set("x",608.25e-6);
set("x span",1219.5e-6);
set("x min",-1.5e-6);
set("x max",1218e-6);
set("y",0);
set("y span",10e-6);
set("y min",-5e-6);
set("y max",5e-6);
set("z",0.375);
set("z span",7.25e-6);
set("y min",-3.25e-6);
set("y max",4e-6);
set("simulation time",40000e-15);  # 40000 fs
set("background material","SiO2 (Glass) - Palik");
set("x max bc","PML");
set("x min bc","PML");
set("y max bc","PML");
set("y min bc","PML");
set("z max bc","PML");
set("z min bc","PML");
# mode source
addmodesource;
```

```
set("injection axis","x");
set("x",-0.1);
set("y",0.1375e-6);
set("y span",2e-6);
set("y min",-0.8625e-6);
set("y max",1.1375e-6);
set("wavelength start",1.55e-6);
set("wavelength stop",1.55e-6);
set("amplitude",1);
# monitors
addpower;
set("name","output_power_upper_bend");
set("monitor type",7);  # 2D z-normal
set("x",1217.5e-6);
set("x span",0);
set("x min",1217.5e-6);
set("x max",1217.5e-6);
set("y",2e-6);
set("y span",1e-6);
set("y min",1.5e-6);
set("y max",2.5e-6);
set("z",0);
addpower;
```

```
set("name","output_power_lower_bend");
set("monitor type",7);  # 2D z-normal
set("x",1217.5e-6);
set("x span",0);
set("x min",1217.5e-6);
set("x max",1217.5e-6);
set("y",-1.95e-6);
set("y span",1e-6);
set("y min",-2.45e-6);
set("y max",-1.45e-6);
set("z",0);
addpower;
set("name","Si_wide_monitor");
set("monitor type",7);  # 2D z-normal
set("x",1190e-6);
set("x span",0);
set("x min",1190e-6);
set("x max",1190e-6);
set("y",0);
set("y span",4e-6);
set("y min",-2e-6);
set("y max",2e-6);
set("z",0);
```

iii. transmission_loop.lsf

```
index = 1.00;
for(0; index<1.51; 0){
setmaterial("X1", {"Refractive Index": (index)});
run;
select("output_power_upper_bend");
T_upper = getresult("output_power_upper_bend","T");
tot_upper = T_upper.T;
select("output_power_lower_bend");
T_lower = getresult("output_power_lower_bend","T");
tot_lower = T_lower.T;
select("Si_wide_monitor");
T_wide = getresult("Si_wide_monitor","T");
tot_wide = T_wide.T;
total_bend = tot_upper + tot_lower;
print(num2str(total_bend,"%.16f") + " " + num2str(tot_wide,"%.16f") + " " +
num2str(tot_upper,"%.16f") + " " + num2str(tot_lower,"%.16f"));
switchtolayout;
index = index +0.01;
}
```

iv. m1_m2_FDE_loop.lsf

```
addmode;
set("solver type",1);
set("x",1180e-6);
set("y",0);
set("y span",10e-6);
set("y min",-5e-6);
set("y max",5e-6);
set("z",1e-6);
set("z span",6e-6);
set("z min",-2e-6);
set("z max",4e-6);
set("background material","SiO2 (Glass) - Palik");
set("y max bc","PML");
set("y min bc","PML");
set("z max bc","PML");
set("z min bc","PML");
set("mesh cells y",800);
set("mesh cells z",800);
index = 1.00;
for(0; index<1.51; 0){
setmaterial("X1", {"Refractive Index": index});
run;
findmodes;
```

```
select("FDE::data::mode1");
m1 = getresult("mode1","neff");
m1_real = real(m1);
m1_imag = imag(m1);
select("FDE::data::mode2");
m2 = getresult("mode2","neff");
m2_real = real(m2);
m2_imag = imag(m2);
print(num2str(m1_real,"%.16f") + " " + num2str(m1_imag,"%.16f") + " " +
num2str(m2_real,"%.16f") + " " + num2str(m2_imag,"%.16f"));
switchtolayout;
index = index +0.01;
}}
```

III-Effective indices for TE0 and TE1 for bimodal waveguide width 660nm

As we said in chapter 3, we need to visualize the effective indices for TE0 and TE1 to calculate the sensitivity. After applying FDE method in Ansys Lumerical, *Figure 18* shows the TE0 and TE1 across the sample index range. As we can see that the change in TE1 in this bimodal waveguide width is high compared to the other widths. And to visualize the phase change for this width, *Figure 19* shows the phase difference. Lastly, we tabulated the difference between the change in effective index for TE1 and the change in effective index for TE0 in *Table 8.* In addition, we added the coupling length and the phase different to the same table.

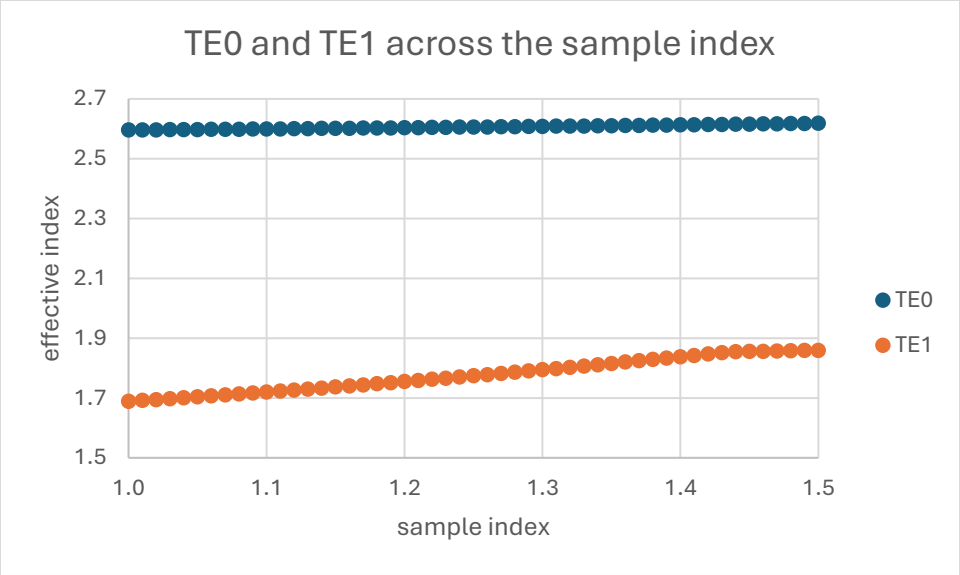

Figure 18 Fundamental and first order modes across the sample index range

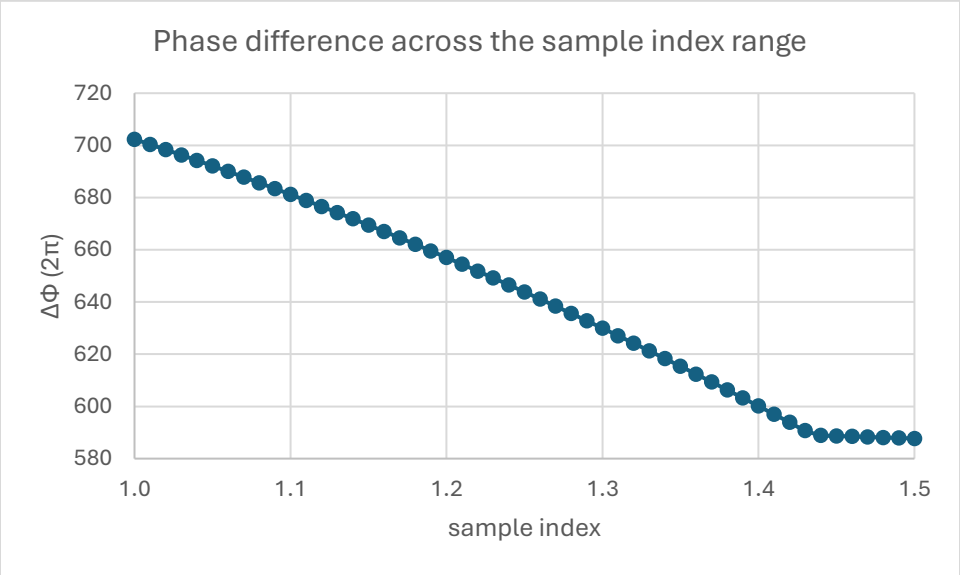

Figure 19 11 Phase difference across the sample index

Table 8 Effective indices for TE0 and TE1, coupling length and phase difference data using FDE across the sample index range

sample index	TE0	TE1	coupling length	ΔΦ (2π)
1.00	2.59606470	1.68883770	854.25146678	702.369
1.01	2.59640611	1.69174447	856.67388693	700.383
1.02	2.59675147	1.69469287	859.14596588	698.368
1.03	2.59710079	1.69768306	861.66858047	696.323
1.04	2.59745412	1.70071519	864.24262015	694.249
1.05	2.59781146	1.70378940	866.86898712	692.146
1.06	2.59817286	1.70690582	869.54859638	690.013
1.07	2.59853832	1.71006457	872.28237581	687.851
1.08	2.59890789	1.71326574	875.07126627	685.658
1.09	2.59928159	1.71650943	877.91622170	683.437
1.10	2.59965944	1.71979571	880.81820926	681.185
1.11	2.60004148	1.72312464	883.77820944	678.903
1.12	2.60042774	1.72649626	886.79721619	676.592
1.13	2.60081823	1.72991061	889.87623711	674.251
1.14	2.60121301	1.73336770	893.01629356	671.88
1.15	2.60161208	1.73686753	896.21842093	669.48
1.16	2.60201550	1.74041008	899.48366874	667.049
1.17	2.60242328	1.74399533	902.81310094	664.589
1.18	2.60283547	1.74762323	906.20779610	662.1
1.19	2.60325209	1.75129370	909.66884764	659.581
1.20	2.60367317	1.75500669	913.19736415	657.032
1.21	2.60409876	1.75876208	916.79446964	654.454
1.22	2.60452889	1.76255977	920.46130381	651.847
1.23	2.60496360	1.76639963	924.19902241	649.211
1.24	2.60540291	1.77028152	928.00879749	646.546
1.25	2.60584687	1.77420527	931.89181776	643.852
1.26	2.60629552	1.77817072	935.84928885	641.129
1.27	2.60674889	1.78217767	939.88243359	638.378
1.28	2.60720702	1.78622591	943.99249224	635.598
1.29	2.60766995	1.79031522	948.18072256	632.791
1.30	2.60813773	1.79444536	952.44839981	629.955
1.31	2.60861039	1.79861606	956.79681640	627.092
1.32	2.60908798	1.80282705	961.22728113	624.202
1.33	2.60957054	1.80707804	965.74111758	621.285
1.34	2.61005811	1.81136871	970.33966120	618.34
1.35	2.61055073	1.81569871	975.02425374	615.369
1.36	2.61104846	1.82006767	979.79623278	612.372
1.37	2.61155133	1.82447515	984.65691087	609.349
1.38	2.61205940	1.82892066	989.60753136	606.301

1.39	2.61257271	1.83340351	994.64916495	603.228
1.40	2.61309131	1.83792266	999.78243069	600.131
1.41	2.61361525	1.84247601	1005.00656463	597.011
1.42	2.61414458	1.84705705	1010.31495490	593.874
1.43	2.61467934	1.85161885	1015.64686866	590.757
1.44	2.61521960	1.85450852	1018.78362950	588.938
1.45	2.61576540	1.85538753	1019.23008299	588.68
1.46	2.61631681	1.85620036	1019.58062032	588.477
1.47	2.61687386	1.85700944	1019.91879739	588.282
1.48	2.61743662	1.85782199	1020.25418088	588.089
1.49	2.61800515	1.85864001	1020.58938503	587.896
1.50	2.61857950	1.85946431	1020.92543293	587.702

IV-Fitting coefficient values for all bimodal waveguide widths

Table 9 Fitting coefficient a, b and c values for all bimodal waveguide widths

Input waveguide width (nm)	Bimodal waveguide width (nm)	a	b	c
450	600	0.992043155	0.265131854	1.15785916
450	625	0.65858298	0.060955605	0.618023836
450	650	0.32901652	0.000310641	1.64732483
450	660	0.258329068	-0.098722872	1.867697472
450	675	0	0.248324823	1.799696215
450	700	0.088052037	0	1.673272603
450	750	0.278411826	0	1.074631366
450	800	0.380941362	0.036789812	0.705122376
450	850	0.441096733	0	1.074728422
350	625	0.678228672	0.000158621	1.16280911
350	650	0.209950026	0.282330914	1.482944451
350	660	0.183081916	0.083496439	1.256592038
350	675	0	0.30044158	1.73391931